Expansion-mediated breakup of bubbles and droplets in microfluidics

Alinaghi Salari [1,2,*] Jiang Xu [1,3,*] Michael C. Kolios [1,4] and Scott S. H. Tsai [1,3,†]

[1]*Institute for Biomedical Engineering, Science and Technology (iBEST), Toronto, Ontario M5B 1T8, Canada*
[2]*Biomedical Engineering Graduate Program, Ryerson University, Toronto, Ontario M5B 2K3, Canada*
[3]*Department of Mechanical and Industrial Engineering, Ryerson University,
Toronto, Ontario M5B 2K3, Canada*
[4]*Department of Physics, Ryerson University, Toronto, Ontario M5B 2K3, Canada*

This paper reports a breakup regime of bubbles and droplets that is caused by a sudden channel expansion in a microfluidic device. In this regime, bubbles or droplets generated at a flow-focusing geometry periodically breakup into smaller bubbles or droplets, respectively, upon entering an expansion. In addition to Capillary number Ca, which is previously shown to govern the dispersion breakup in such geometries, we find that, at a high-inertia regime, the Weber number We also plays a significant role in specifying the transition from non-breakup to breakup regimes. Furthermore, we identify different periodic breakup modes, for example, symmetric and asymmetric breakup, which are dictated by the Ohnesorge number. A power law of $f^{0.5} \propto We^{0.1}Ca^{0.2}$, where f denotes the frequency at which the dispersions arrive at the expansion region, governs when the droplets and bubbles breakup. This power law highlights the importance of inertia to the dispersion breakup in an expansion-mediated geometry. Our results demonstrate that, without modifying the geometry and by only tuning several dimensionless parameters related to the fluid flow, a microchannel expansion region can produce mono-, bi-, or tri-disperse bubble or droplet populations. These discoveries may find utility in the design of multi-disperse bubble or droplet populations using microfluidics.

I. INTRODUCTION

When two immiscible fluids meet at a microfluidic junction, interfacial instabilities, such as Rayleigh-Plateau, causes one fluid to break into a series of dispersions—bubbles or droplets [1]. Due to many applications that utilize bubbles and/or droplets, the formation strategies [2,3] and breakup regimes [4,5] of droplets and bubbles impact fields such as emulsion and colloid formation [6,7], bioagent encapsulation [8], polymerase chain reaction (PCR) [9], ultrasound contrast agent production [10], and food processing [11]. The primary droplets and bubbles, which are formed when the two immiscible fluids first meet in a microfluidic device, are also observed to break into secondary droplets and bubbles in various geometries, including at microfluidic T junctions [4,12,13], and constrictions [14]. In all of these breakup cases, the droplet or bubble is physically obstructed, compressed, and then eventually broken into smaller droplets or bubbles, respectively.

One important dimensionless number describing the generation of bubbles and droplets in a microfluidic channel is the Capillary number $Ca = \mu v / \sigma$, where μ, v, and σ are the liquid viscosity,

---

*These author contributed equally to this work.
†scott.tsai@ryerson.ca

liquid flow rate, and interfacial tension, respectively. Typically, the breakup of droplets and bubbles flowing in a microfluidic channel occurs at relatively low Capillary numbers, where $Ca = O(10^{-2})$ [5,15–18]. Hashimoto *et al.* shows that, in a system of droplets with sufficiently low Capillary number and low interfacial tension, $\sigma = O(10^{-1})$ mN m^{-1}, driven in a microfluidic Hele-Shaw cell (HSC), capillary and shear-driven instabilities induce the breakup of droplets [15]. In such a HSC configuration, droplets generated at a flow-focusing junction are delivered into an expanded channel that is fifty times wider than its height (so that the two-dimensional flow in the HSC obeys Darcy's law, mathematically equivalent to the flow in a porous medium). The timescale required for these instabilities to evolve is relatively long, $t = O(10)$ ms [15], compared with another regime in a similar geometry studied by Vecchiolla *et al.*, which is shown to have a shorter breakup timescale, $t = O(0.1)$ ms [19]. In the latter regime, however, bubbles split near the entrance of the expansion region, at a higher Capillary number $Ca = O(10^{-1})$ and at a higher rate of about 10 000 bubbles per second. Vecchiolla *et al.* also show that bubbles can either flow undisturbed, break periodically into equal-sized daughter bubbles, or break irregularly depending on the value of Capillary number. They demonstrate that periodic asymmetric breakup, where the daughter bubbles are of unequal sizes, can only be achieved if an asymmetric geometry of the expansion region is employed. In all designs reported by Vecchiolla *et al.*, the channel width at the expansion region increases at an angle less than 90°, and thus, as bubbles enter the expansion region, their travelling speed decreases gradually. In such a geometry, the competition between interfacial tension and the viscous stress imposed by the continuous flow appears to govern the periodic breakups, and thus, the Capillary number is the major dimensionless number in the power-law relationship [19].

Here, we use a flow-focusing microfluidic design, coupled with a sudden increase in channel width, to further study different flow regimes in expansion-mediated geometries, and quantify symmetric and asymmetric breakup of bubbles. In contrast with the geometry used by Vecchiolla *et al.*, in our microfluidic design, the channel width increases at 90° at the expansion region, which causes the speed of the bubbles to decrease immediately once they enter the expansion region. This sudden increase in the channel width causes the effect of inertia to become critical, especially at the entrance of the expansion region. Therefore, we find that the inertial force—as quantified by the dimensionless Weber number We—significantly contributes to determining the transition from non-breakup to breakup regimes. In addition to mono-disperse and bi-disperse output populations reported by Vecchiolla *et al.*, we observe an additional regime, where the microfluidic system produces periodic tri-disperse populations. To better understand the breakup mechanism, we perform dimensional analyses to characterize the competition between governing physical effects, which are inertia, viscosity, and interfacial tension. Our finding suggests that the dimensionless Ohnesorge number Oh defines the breakup transition from symmetric to asymmetric modes. We also ask the additional question of what happens when we flow different liquid droplets, instead of bubbles, into the expansion, and we find the same flow regimes as in our bubble experiments. Finally, we find that all of our experimental results follow a power law, $f^{0.5} \propto We^{0.1}Ca^{0.2}$, which precisely predicts when dispersions will breakup. The dimensionless theoretical framework presented here can be applied to other expansion-mediated geometries and various types of fluids to help engineer multi-disperse populations for applications such as producing complex wet foams [20–22], and self-assembling hyperuniform materials [23,24].

II. METHODOLOGY

The microfluidic device we use for the generation of air microbubbles is shown in Figs. 1(a) and 1(b), where the two flows meet at a flow-focusing cross-junction. The same geometry is used to generate droplets. The dispersed phase, which is a gas in bubble experiments and a liquid in droplet experiments, is supplied by using a pressure regulator (Omega Engineering, USA) and a pressure pump (Fluigent, USA), respectively. The aqueous continuous phase is infused by a syringe pump (Harvard Instruments, USA).
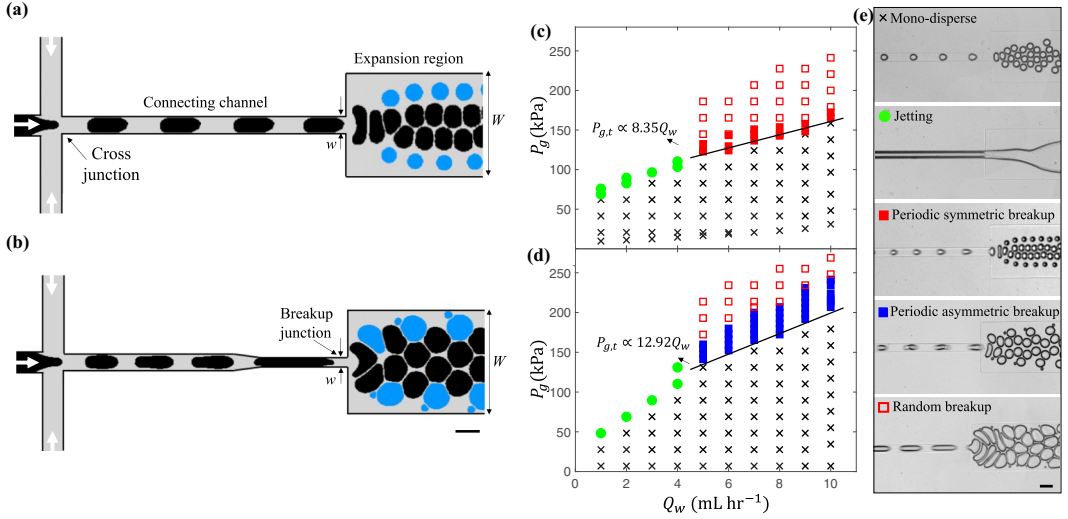
FIG. 1. (a), (b) Schematic diagram of the device showing a microfluidic flow-focusing geometry coupled with an expansion region at the breakup junction. First, air microbubbles (shown in black) are generated at the flow-focusing cross-junction and then travel through the connecting channel, which leads to the expansion region. The two geometries used in this study have identical dimensions except at the breakup junction. In panel (a), the connecting channel has a uniform width $w = 40$ μm. In panel (b), the connecting channel width tapers from 40 μm to a width $w = 20$ μm at the breakup junction, over a 100 μm distance that begins 300 μm upstream from the breakup junction. At specific values of certain geometrical and flow parameters, the microbubbles are squeezed at the entrance of the expansion region, and thus periodically break into smaller daughter bubbles (shown in blue). w and W represent the widths of the breakup junction and expansion region, respectively. The continuous and dispersed phases are shown in gray and black, respectively. (c)–(e) Different flow regimes observed in our bubble-generation experiment. Here, the geometry has the breakup junction width $w = 40$ μm and the experiment uses two different aqueous solutions: (c) Aq-b1; (d) Aq-b2 (see Table I). At an aqueous flow rate $Q_w > 5$ mL hr^{-1}, increasing the gas pressure P_g eventually leads to the transition from mono-disperse bubbles to periodic symmetric or asymmetric breakup, and then random breakup. (e) Microscope images of each flow regime in this experiment. The scale bars represent 50 μm.

The aqueous continuous phase in our study consists of different mixing ratios of glycerol, deionized water, Pluronic F-68, and sodium dodecyl sulfate (SDS). We tune the viscosity and interfacial tension by adjusting the amount of glycerol and SDS in the aqueous solution, respectively. The viscosity is measured by using a Cannon-Fenske Routine viscometer, and the interfacial tension is measured by using the pendant drop method [25]. We use the following three different aqueous solutions for bubble generation experiments: Aq-b1 is a mixture of glycerol, DI water, and Pluronic F-68 at a 0.5:1:1 volume ratio, which has a liquid-air interfacial tension $\sigma = 41.9$ mN m^{-1} and viscosity $\eta = 3.23$ mPa s; Aq-b2 is the mixture of glycerol, DI water, and Pluronic F-68 at a 1:1:1 volume ratio, plus 1 wt. % SDS, and has liquid-air interfacial tension $\sigma = 37.6$ mN m^{-1} and viscosity $\eta = 6.45$ mPa s; Aq-b3 is a mixture of glycerol, deionized water, and Pluronic F-68 at a 1:1:1 volume ratio, and has liquid-air interfacial tension $\sigma = 40.6$ mN m^{-1} and viscosity $\eta = 5.16$ mPa s. Table I shows a list of the aqueous solution abbreviations and their properties that we use in the bubble experiments. It also contains the properties of solutions that we use in the droplet experiments, which are mentioned later in the text.

We fabricate the microfluidic device by using photolithography followed by soft lithography [26]. All microfluidic channels have a height of 26 μm. The molded polydimethylsiloxane (PDMS) replicate of the microfluidic channels is then bonded to a glass slide by plasma treatment.

TABLE I. List of aqueous solutions and their properties used in our experiments.

Experiment	Aqueous solution	Interfacial tension σ (mN m^{-1})	Viscosity η (mPa s)
Air bubble	Aq-b1	41.9	3.23
	Aq-b2	37.6	6.45
	Aq-b3	40.6	5.16
Dodecane droplet	Aq-d1	8.61	3.23
	Aq-d2	5.82	6.45
	Aq-d3	9.52	5.16
Mineral oil droplet	Aq-m1	1.83	15.41
	Aq-m2	1.48	20.36
	Aq-m3	2.84	21.98

Once dispersions are generated at the cross-junction, they travel through the connecting channel before entering the expansion region. The connecting channel is designed to be long (850 μm) to ensure that the dispersion generation at the cross-junction does not interfere with breakup at the expansion region.

We design two microfluidic geometries that have identical cross-junction width, connecting channel length, and expansion region width, and differ only by the breakup junction geometry [Figs. 1(a) and 1(b)]. The first geometry has a uniform breakup junction width $w = 40$ μm [Fig. 1(a)]. The second geometry has a breakup junction width $w = 20$ μm. The connecting channel width of this geometry tapers, at a constant angle, from 40 μm to $w = 20$ μm over a 100 μm distance that begins 300 μm upstream from the breakup junction [see Fig. 1(b)].

III. RESULTS AND DISCUSSIONS

In a typical cross-junction bubble generation microfluidic device, gas pressure, interfacial tension, and the aqueous solution flow rate and viscosity are the main parameters governing the size of the bubbles pinched off from the gas thread [27,28]. In these systems, the output of the device is either mono-disperse (or under specific conditions poly-disperse [29]) bubbles or jets (governed by nonlinear instabilities [30,31]). These regimes can also be observed in our bubble breakup experimental results. As shown in Figs. 1(c) and 1(d), at low aqueous solution flow rates $Q_w < 5$ mL hr^{-1} and relatively low gas pressure P_g, we observe mono-disperse bubbles, as expected [28,32]. For a gas pressure $P_g \sim 50$–100 kPa the gas thread reaches the expansion region (also called jetting regime) and no bubble generation occurs.

However, as shown in Figs. 1(c) and 1(d), at relatively high liquid flow rates $Q_w > 5$ mL hr^{-1}, we observe a third regime at high gas pressures P_g, where mono-disperse bubbles generated at the cross-junction breakup into two smaller daughter bubbles once they enter the expansion region (see Supplemental Material Video1 and Video2 [33]). At this point increasing the gas pressure P_g causes the periodic bubble breakup regime to transition into a random breakup regime. Here, the term "periodic" denotes the phenomenon of a constant number ratio of breakup to non-breakup bubbles at the expansion region (for example, one out of every three bubbles breaks into daughter bubbles). Random breakup refers to the case where this number ratio is not constant. Additionally, we observe both symmetric (i.e., roughly-equal-sized daughter bubbles) and asymmetric (i.e., unequal-sized daughter bubbles) breakup. We find the experimental best fit transition lines $P_{g,t} \propto 8.35Q_w$ and $P_{g,t} \propto 12.92Q_w$ for the transition between mono-disperse to periodic regimes in Figs. 1(c) and 1(d), respectively.

We note that the breakup regime studied here is different from the bifurcation of bubble sizes observed at a flow-focusing device [29], where at the orifice, the system produces sequences of
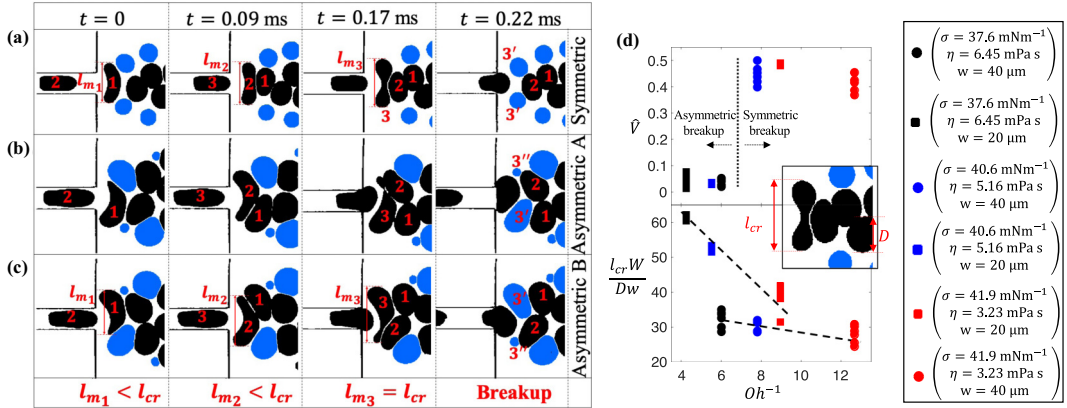
FIG. 2. (a)–(c) Images of different modes of periodic breakup occurring at the entrance of the expansion region. Intact bubbles are shown in black, whereas daughter bubbles that result from breakup are in blue. (a) The periodic symmetric mode, and (b), (c) the periodic asymmetric mode. The asymmetric mode can be further categorized into two sub-modes A and B, which occur consecutively one after another, meaning that every asymmetric A sub-mode is followed by an asymmetric B sub-mode. As shown, the presence of the pre-arrived bubbles 1 and 2 is crucial for the breakup of bubble 3. Each bubble is elongated to its maximum length l_m once it enters the expansion region. In a sequence of three arriving bubbles, only one bubble is elongated to its critical length of l_{cr}, at which point breakup occurs. The images in panel (a) are from experiments that use Aq-b1, and in panels (b), (c) Aq-b2 is used. (d) A plot of the volume ratio of the daughter bubbles (top graph), and dimensionless critical length immediately before breakup (bottom graph) versus the inverse Ohnesorge number Oh^{-1}. The value of Oh^{-1} determines the periodic breakup mode. As shown, for each geometry, a decrease in l_{cr}/D is observed by increasing Oh^{-1}, suggesting that the effect of shear force becomes significant in asymmetric breakup. However, in the symmetric mode, shear appears to be a secondary dominant force. All data depicted in panel (d) are collected at the transition pressure of $P_{g,t}$, the point at which the mono-disperse regime changes to the periodic breakup regime [see Figs. 1(c) and 1(d)].

bubbles with two (or more) different sizes. In such a system, bubbles of different sizes are pinched off from the gas thread, whereas in our system, mono-disperse bubbles breakup at the expansion, regardless of where and how they are generated.

In both of our geometries, the liquid flow velocity in the expansion region is approximately an order of magnitude lower than the velocity in the connecting channel. The lower velocity dictates that once the bubbles enter the expansion region, they decelerate significantly and mimic slow-moving obstacles that cause the flow streamlines to deviate to the sides of the expansion region. If the subsequent bubble enters the expansion region before the streamlines are relaxed to their original position, the subsequent bubble becomes squeezed, elongates, and breaks into daughter bubbles [see, for example Fig. 2(a)].

All bubbles experience a high degree of shear and inertia at the entrance of the expansion region, which causes them to become elongated to a maximum length l_m perpendicular to the average flow direction. At this position, if the pro-elongation inertial and shear forces overcome the interfacial tension force, the bubble will break up. We denote the corresponding critical bubble length l_{cr}, as the measured length of the bubble right before breakup. Based on our observations, in a periodic breakup regime, the number of bubbles entering the expansion region between two successive breakups for all experiments is within the range of 2, where one of every two bubbles break, to 5, when one of every five bubbles break.

Figures 2(a)–2(c) show an example sequence of bubble breakup for both symmetric and asymmetric modes, where the period is three. As shown, no breakup occurs for bubbles labeled 1 and 2, which have maximum length $l_m < l_{cr}$ as they regain their original shape after moving

downstream. This means that not all bubbles break. The presence of pre-arrived bubbles 1 and 2 at the expansion region is a key factor for the breakup of an arriving bubble 3.

As shown in Fig. 2(a), bubble 2 temporarily (based on our observations, $\sim 10^{-2}$ ms) blocks the path of bubble 3 at the entrance of the expansion region. Thus, for this time period, the role of bubble 2 is physically similar to that of the channel wall in a T-junction geometry [4,12].

In contrast to T junctions, where asymmetrical channel dimensions lead to asymmetrical breakup [5,34], in our device, both symmetrical and asymmetrical breakup can occur in a symmetrical microchannel geometry. The type of breakup depends on the flow conditions. Asymmetric A and B regimes shown in Figs. 2(b) and 2(c), respectively, are the two sub-modes of asymmetric breakup that occur consecutively. Every asymmetric A sub-mode is followed by an asymmetric B sub-mode. The difference between these two sub-modes is the location of breakup. As shown in Figs. 2(b) and 2(c), the breakup location of bubble 3 is shifted towards one side of the expansion region, and the larger daughter bubble 3′ flows adjacent to bubble 1 while the smaller daughter bubble 3″ flows adjacent to bubble 2.

Inspired by the observations of droplet breakup occurring at microfluidic T junctions [12,35,36], we hypothesize that, in our system, the major force competition governing breakup is between the inertial force, which scales as $\rho v^2 D^2$, and interfacial tension force, which scales as σD. Here, ρ, v, and D are the liquid density, average velocity at the connecting channel, and the (projected) initial diameter of the bubble, respectively. We note that the actual bubble diameter is different from the projected diameter because the bubble diameter, upon exiting the device, is larger than the channel height, and thus the bubble within the microchannel is squeezed from its top and bottom. Therefore, we calculate the actual volume of the bubbles by using a mathematical approach that is explained elsewhere in the literature [7]. Briefly, the volume of a discoid bubble is approximately equal to the volume of an undeformed bubble minus two caps. By measuring the discoid diameter, we can calculate the volume of the bubble.

To test our hypothesis, we define the Weber number as $We = \rho v^2 D \sigma^{-1}$ and map the values of We for the two geometries that correspond to the breakup regime. We observe that the breakup regime is $2 < We < 8$ for the geometry with junction width $w = 40$ μm, and $10 < We < 45$ for the geometry with junction width $w = 20$ μm. We are unable to run experiments for $We > 8$, and $We > 45$ in the two geometries, respectively, due to the large pressure at the tubing connections. Thus, we find the non-breakup to breakup critical Weber number $We_{cr} \approx 2$ and $We_{cr} \approx 10$ for the two geometries, respectively.

In our system, since mono-disperse bubbles are first generated upstream in the same microfluidic device, ensuring that $We > We_{cr}$ causes the generation of bubbles of specific size and at generation frequencies that can lead to periodic breakup. Thus, $We > We_{cr}$ is the only requirement for breakup to occur in our system. If bubbles are first generated elsewhere, and then transferred into a microfluidic device equipped with an expansion geometry similar to ours, then there will be a minimum ejection rate (in our experiments it is within the range 10–30 kHz), at which the bubbles are required to enter the expansion region, in addition to having $We > We_{cr}$, to ensure that breakup occurs. This range ensures that the bubble enters the expansion region before the streamlines are relaxed to their original position. This is different from the case of breakup in T-junction geometries, where the ejection rate of bubbles does not play a significant role. In a hypothetical case of very low ejection rate (not shown here), the probability of breakup would be minimized. In such a case, We_{cr} would be much higher than the values reported here, and the symmetric breakup would be dominant over the asymmetric breakup. Maintaining a small value of the design ratio, W/w, would also help in achieving breakup at lower We_{cr}. In contrast, assuming a very high ejection rate of bubbles, the breakup regime would still be achievable at a We_{cr} value that is in the same range as those reported here. At this extreme case, the breakup would have to be asymmetric, since the expansion region would be fully occupied by bubbles, and the arriving bubbles would be pushed to the sides of the expansion region [37].

In order to characterize symmetric and asymmetric periodic breakup modes, we define the Ohnesorge number $Oh = \mu/\sqrt{\rho \sigma w}$, which compares the strength of viscosity to inertia and

interfacial tension. Our results show that, when $Oh^{-1} < 7$, bubbles entering the expansion region move periodically to the sides of the expansion. This is due to an abrupt decrease in the liquid speed that causes the bubbles to slow down and push against each other [Figs. 2(b) and 2(c)]. If a bubble becomes squeezed and the shear stress overcomes the interfacial tension, it will stretch beyond l_{cr}, and eventually break asymmetrically into two daughter bubbles with unequal sizes. This is shown in Fig. 2(d), when $Oh^{-1} < 7$, and for all different aqueous solutions, the daughter bubbles' volume $\hat{V} < 0.1$, where the dimensionless volume $\hat{V}$ is the volume ratio of the smaller daughter bubble to the intact bubble.

Asymmetric breakup can only occur if the inertial force is relatively low, whereas, at high inertial forces, the breakup becomes more symmetric, meaning that bubbles break into two equal size daughter bubbles. In this situation, the flow inertia is strong enough to push the preceding bubbles away from the breakup junction, prior to the arrival of the subsequent bubble. This causes the breaking bubble to experience two equal forces, and thus the bubble breaks into two roughly-equal-sized daughter bubbles. This observation corresponds to $\hat{V} \approx 0.4$–0.5 when $Oh^{-1} > 7$ [Fig. 2(d)]. Therefore, we define a critical Oh^{-1} number $Oh_{cr}^{-1} = 7$ that roughly separates symmetric and asymmetric breakup modes. This finding enables us to design a tri-disperse bubble generation device, without adding asymmetry to the geometry as in Vecchiolla *et al.* [19].

Our observations also reveal that the critical bubble length l_{cr} is in the range $1.7 < l_{cr}/D < 2.4$ and depends on the Ohnesorge number Oh scaling as $Oh \propto l_{cr}W/Dw$. As shown in lower graph of Fig. 2(d), in both geometries, the dimensionless critical length l_{cr}/D of an asymmetric breakup is greater than in symmetric breakup. The value of l_{cr}/D is directly proportional to the magnitude of viscous stress. This suggests that, in asymmetric breakup, shear stress contributions are comparable to, and in some cases more significant than, inertial contributions. In symmetric breakup, however, inertia is the dominant contributor. Therefore, we also need to consider the Capillary number in order to fully characterize the breakup over different experimental conditions. Note that, for larger values of W/w, a larger inertial force is required to trigger the breakup regime. This explains why We_{cr} is lower in experiments with the geometry $w = 40\ \mu$m than those with $w = 20\ \mu$m. Our observations also suggest that, once the periodic breakup regime begins, geometries with smaller aspect ratio W/w induce a more stable breakup, and thus the transition between symmetric and asymmetric modes is less dependent on the flow properties. Furthermore, Fig. 2(d) reveals that an increase in the bubble size will shift the breakup regime in each geometry towards the symmetric mode, as opposed to the breakup of smaller bubbles that will be shifted towards the asymmetric mode.

Figure 3 shows the bubble size distributions at the outlet of our device with a maximum bubble production rate of $1.6 \times 10^5\ \mathrm{s}^{-1}$. When no breakup occurs, only a monodisperse size distribution is obtained [Fig. 3(a)]. By only adjusting the flow rate and gas pressure, however, we are able to achieve bubble breakup at the expansion region to yield a multi-disperse population at the outlet [see Figs. 3(b) and 3(c)].

It is known that the mechanisms governing the formation of bubbles and droplets in microfluidic devices are similar [2,38], so we hypothesize that expansion-mediated breakup mechanisms may also be similar. We thus design analogous experiments that use oil, i.e., dodecane and mineral oil, as the dispersed phase, and the same continuous phase as in the bubble experiments, albeit with different amounts of added glycerol. By changing the glycerol ratio in the continuous phase, we study the droplet breakup over a range of different viscosities.

We use aqueous solutions Aq-d1 with liquid-liquid interfacial tension $\sigma = 8.61\ \mathrm{mN\ m^{-1}}$, Aq-d2 with liquid-liquid interfacial tension $\sigma = 5.82\ \mathrm{mN\ m^{-1}}$, and Aq-d3 with liquid-liquid interfacial tension $\sigma = 9.52\ \mathrm{mN\ m^{-1}}$ for the dodecane droplet experiments. In mineral oil droplet experiments, we use the following aqueous solutions: Aq-m1, is a mixture of glycerol, DI water, and Pluronic F-68 at a 3:1:1 volume ratio, which has a liquid-liquid interfacial tension $\sigma = 1.83\ \mathrm{mN\ m^{-1}}$ and viscosity $\eta = 15.41\ \mathrm{mPa\ s}$; Aq-m2 is the mixture of glycerol, DI water, and Pluronic F-68 at a 4:1:1 volume ratio, plus 1 wt. % SDS, and has a liquid-liquid interfacial tension $\sigma = 1.48\ \mathrm{mN\ m^{-1}}$
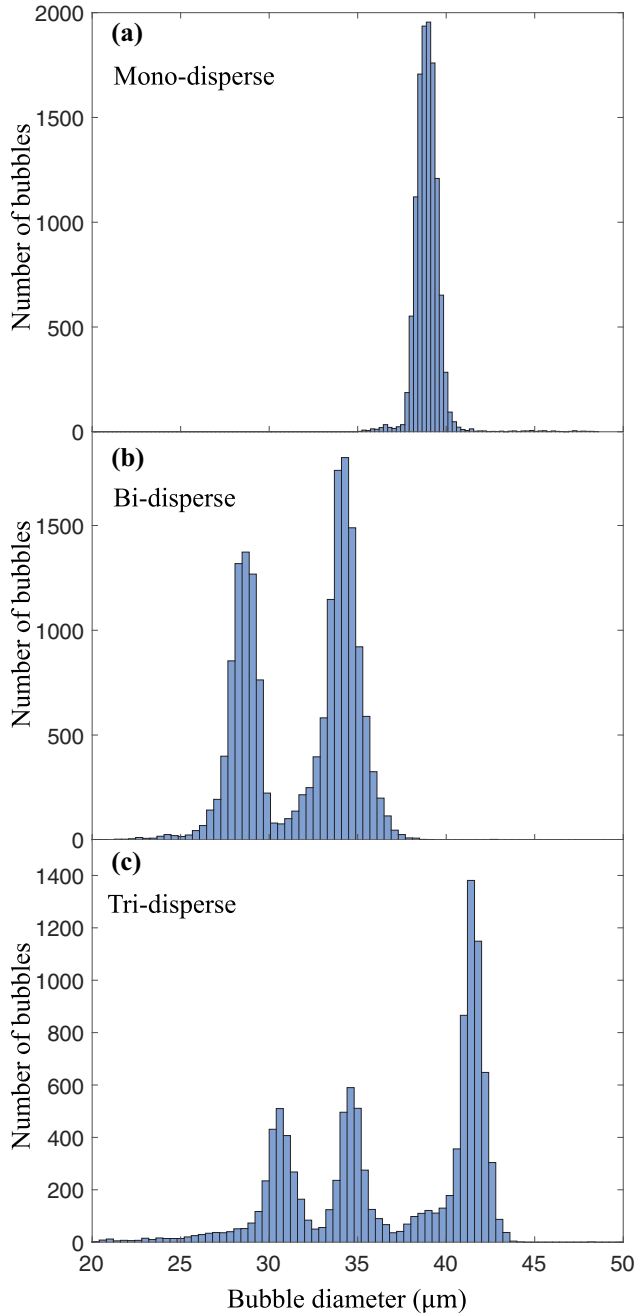
FIG. 3. Different output populations obtained in our bubble-generation experiments. Here, the geometry with the breakup junction width $w = 40$ μm and continuous phase Aq-b1 is used. (a) $P_g = 100$ kPa, $Q_w = 5$ mL hr^{-1}; (b) $P_g = 160$ kPa, $Q_w = 10$ mL hr^{-1}; (c) $P_g = 180$ kPa, $Q_w = 10$ mL hr^{-1}. As shown, using a single geometry, we obtain (a) mono-disperse, (b) bi-disperse, or (c) tri-disperse populations only by controlling the aqueous phase flow rate and gas pressure. In panels (b) and (c), one in every three bubbles breaks. Therefore, the number of intact bubbles in panel (b) is approximately equal to the number of daughter bubbles, and in panel (c) the number of intact bubbles is approximately two times greater than the number of daughter bubbles.
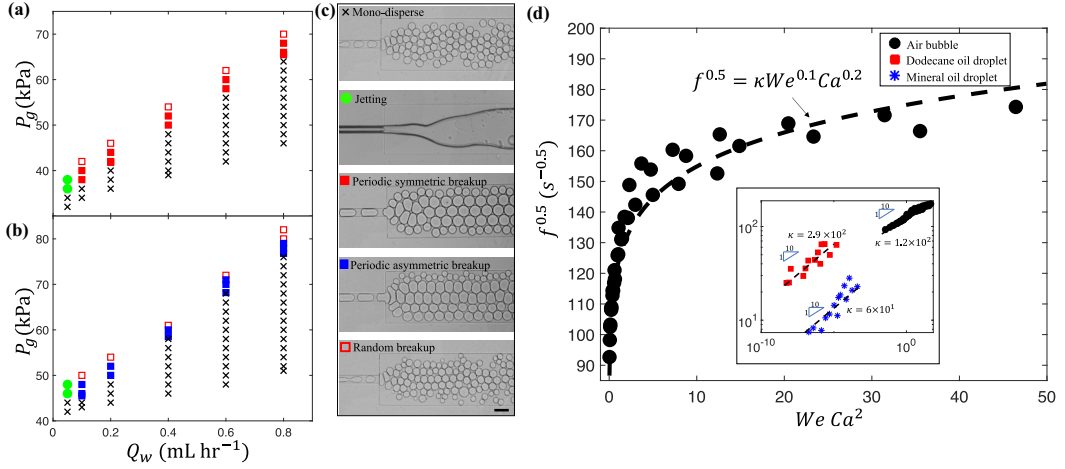
FIG. 4. (a)–(c) Different flow regimes observed in our dodecane droplet generation experiment for the geometry of breakup junction width $w = 40$ μm and two different aqueous solutions: (a) Aq-d1; (b) Aq-d2 (see Table I). To be consistent with the results presented in Figs. 1(c) and 1(d), here we report the dispersed phase pressure versus continuous phase flow rate. At an aqueous flow rate $Q_w > 0.1$ mL hr^{-1}, increasing the oil pressure P_g leads to the transition from mono-disperse bubbles to periodic symmetric or asymmetric breakup, and then random breakup. (c) Microscope images of each flow regime in this experiment. Droplet breakup regimes exhibit similar trends of mono-disperse, periodic symmetric, and asymmetric breakup that are observed in bubble breakup experiments [see Figs. 1(c) and 1(d)]. (d) The frequency f at which dispersions arrive at the expansion region versus the product of Weber number and the squared Capillary number, $WeCa^2$. Here, the dashed curve $\kappa We^{0.1}Ca^{0.2}$ is fit to the experimental data points obtained from bubble experiments. The inset shows a log-log plot of f versus $WeCa^2$, where the dashed line shows the scaling, $f^{0.5} = \kappa We^{0.1}Ca^{0.2}$. All data depicted here are collected at the transition pressure $P_{g,t}$, at which point the mono-disperse regime changes to the periodic breakup regime [see Figs. 1(c), 1(d) and 4(a), 4(b)]. The proportionality constants κ for bubble, dodecane oil droplet, and mineral oil droplet experiments are 1.2×10^2, 2.9×10^2, and 6.0×10^1, respectively. The bubble and droplet experimental results show a good agreement with the scaling, $f^{0.5} \propto We^{0.1}Ca^{0.2}$. The scale bar represents 50 μm.

and viscosity $\eta = 20.36$ mPa s; Aq-m3 is a mixture of glycerol, DI water, and Pluronic F-68 at a 4:1:1 volume ratio, and has a liquid-liquid interfacial tension $\sigma = 2.84$ mN m^{-1} and viscosity $\eta = 21.98$ mPa s. These properties are listed in Table I.

In Figs. 4(a) and 4(b), when the liquid flow rate $Q_w > 0.1$ mL hr^{-1}, increasing P_g causes droplets to transition from mono-disperse to periodic breakup. Here, mono-disperse oil droplets generated at the cross-junction breakup into two smaller daughter droplets once they enter the expansion region (see Supplemental Material Video3 and Video4 [33]). At this point, continuing increase of oil injection pressure P_g causes the periodic droplet breakup regime to enter into a random breakup regime. Comparing Figs. 1(c) and 1(d) with 4(a) and 4(b), we can observe identical flow regimes and similar transitions between different regimes in both bubble and droplet experiments.

In our system, in addition to the fluid properties and microchannel design, dispersed phase inlet pressure and the continuous phase flow rate are the main design parameters that control the generation of either mono-disperse, bi-disperse (i.e., the result of periodic symmetric breakup), or tri-disperse microbubbles and droplets (i.e., the result of periodic asymmetric breakup).

In our experiments, the transition pressure $P_{g,t}$, at which the dispersion behavior moves from the mono-disperse regime to the periodic breakup regime, has a linear relationship with the continuous phase flow rate [see Figs. 1(c), 1(d) and 4(a), 4(b)]. Since dispersions are generated at a cross-junction in our device, this linear relationship implies that the inlet pressure of dispersed phase is

related to the frequency at which the dispersions arrive at the expansion region, as $P_{g,t} \propto f^{0.5}$ [32]. This is also supported by our observations.

As shown in Fig. 4(d), we find experimentally that this frequency follows the scaling $f^{0.5} = \kappa We^{0.1}Ca^{0.2}$, where $\kappa = 1.2 \times 10^2$, 2.9×10^2, and 6.0×10^1 for the bubble, dodecane oil droplet, and mineral oil droplet data points, respectively. This scaling law is reinforced when the data points are plotted on a log-log graph [inset of Fig. 4(d)]. Here, we change the variables v, μ, and σ in our experiments, and since $We^{0.1}Ca^{0.2}$ scales as $v^{0.4}$, $\mu^{0.2}$, and $\sigma^{-0.3}$, the relative importance of each parameter can be inferred. The variation between the pre-factor κ associated with the data from bubble and droplet experiments may be attributed to the differences in dispersed phase properties (e.g., viscosity contrast of the fluids [39]) in the bubble, dodecane oil droplet, and mineral oil droplet experiments. Experiments with fluids having a wider range of properties would be required to fully characterize the κ values and can be investigated in future studies.

Figure 4(d) reveals that, for both droplets and bubbles, the transition into the breakup regime is highly dependent on the continuous phase flow velocity. This is a major difference between the expansion-mediated and T-junction-induced breakup phenomena. However, the competition between the viscous force, which promotes breakup, and the interfacial tension force, which inhibits breakup, is similar in both expansion-mediated and T-junction systems [5,12,39]. Figure 4(d) also shows that, for relatively small values of $WeCa^2$, the transition into the breakup regime becomes almost independent of the frequency of dispersions arriving at the expansion region, whereas, for relatively large values of $WeCa^2$, the transition is governed mainly by the magnitude of $f^{0.5}$.

IV. CONCLUSIONS

In this manuscript, we extend the idea of formation multi-disperse bubbles at a microfluidic expansion [19], by performing dimensional analyses to quantitatively identify the main physical parameters governing this phenomenon. This microchannel expansion breakup regime is based on bubble- or droplet-induced obstruction occurring in a microfluidic expansion region. We find that the physical breakup mechanisms of both bubbles and droplets in this regime are identical. We also define and experimentally fit the relevant dimensionless numbers and control the output of the device to produce mono-disperse, bi-disperse, and tri-disperse bubble or droplet populations without modifying the microfluidic geometry. We believe the results presented in this article are valuable for a wide range of audiences in the fields of bubble- or droplet-based microfluidics for various applications in medicine [40], science [41], and technology [11,24,42].

[1] L. Rayleigh, On the instability of jets, Proc. London Math. Soc. **s1-10**, 4 (1878).

[2] P. Garstecki, M. J. Fuerstman, H. A. Stone, and G. M. Whitesides, Formation of droplets and bubbles in a microfluidic T-junction—Scaling and mechanism of break-up, Lab Chip **6**, 437 (2006).

[3] B. Dollet, W. Van Hoeve, J. P. Raven, P. Marmottant, and M. Versluis, Role of the Channel Geometry on the Bubble Pinch-Off in Flow-Focusing Devices, Phys. Rev. Lett. **100**, 034504 (2008).

[4] A. M. Leshansky and L. M. Pismen, Breakup of drops in a microfluidic T-junction, Phys. Fluids **21**, 023303 (2009).

[5] M. Samie, A. Salari, and M. B. Shafii, Breakup of microdroplets in asymmetric T junctions, Phys. Rev. E **87**, 053003 (2013).

[6] V. Gnyawali, B.-U. Moon, J. Kieda, R. Karshafian, M. C. Kolios, and S. S. H. Tsai, Honey, I shrunk the bubbles: Microfluidic vacuum shrinkage of lipid-stabilized microbubbles, Soft Matter **13**, 4011 (2017).

[7] Z. Nie *et al.*, Emulsification in a microfluidic flow-focusing device: Effect of the viscosities of the liquids, Microfluid. Nanofluidics **5**, 585 (2008).

[8] J. Xu *et al.*, Controllable microfluidic production of drug-loaded PLGA nanoparticles using partially water-miscible mixed solvent microdroplets as a precursor, Sci. Rep. **7**, 4794 (2017).

[9] Z. Chen, P. Liao, F. Zhang, M. Jiang, Y. Zhu, and Y. Huang, Centrifugal micro-channel array droplet generation for highly parallel digital PCR, Lab Chip **17**, 235 (2017).

[10] K. Ferrara, R. Pollard, and M. Borden, Ultrasound microbubble contrast agents: Fundamentals and application to gene and drug delivery, Annu. Rev. Biomed. Eng. **9**, 415 (2007).

[11] K. W. Soli *et al.*, Decontamination of fresh produce by the use of slightly acidic hypochlorous water following pretreatment with sucrose fatty acid ester under microbubble generation, Food Control **21**, 1240 (2010).

[12] A. M. Leshansky, S. Afkhami, M. C. Jullien, and P. Tabeling, Obstructed Breakup of Slender Drops in a Microfluidic T Junction, Phys. Rev. Lett. **108**, 264502 (2012).

[13] M.-C. Jullien, M.-J. Tsang Mui Ching, C. Cohen, L. Menetrier, and P. Tabeling, Droplet breakup in microfluidic T-junctions at small capillary numbers, Phys. Fluids **21**, 072001 (2009).

[14] R. Lespiat, S. Cohen-Addad, and R. Höhler, Jamming and Flow of Random-Close-Packed Spherical Bubbles: An Analogy with Granular Materials, Phys. Rev. Lett. **106**, 148302 (2011).

[15] M. Hashimoto, P. Garstecki, H. A. Stone, and G. M. Whitesides, Interfacial instabilities in a microfluidic Hele-Shaw cell, Soft Matter **4**, 1403 (2008).

[16] Y. Wu, T. Fu, C. Zhu, Y. Lu, Y. Ma, and H. Z. Li, Asymmetrical breakup of bubbles at a microfluidic T-junction divergence: Feedback effect of bubble collision, Microfluid. Nanofluidics **13**, 723 (2012).

[17] A. Nishimura, A. Schmit, L. Salkin, L. Courbin, and P. Panizza, Breakup of confined drops against a micro-obstacle: An analytical model for the drop size distribution, Microfluid. Nanofluidics **21**, 1 (2017).

[18] Y. Lu, T. Fu, C. Zhu, Y. Ma, and H. Z. Li, Dynamics of bubble breakup at a T junction, Phys. Rev. E **93**, 022802 (2016).

[19] D. Vecchiolla, V. Giri, and S. L. Biswal, Bubble-bubble pinch-off in symmetric and asymmetric microfluidic expansion channels for ordered foam generation, Soft Matter **14**, 9312 (2018).

[20] M. Hashimoto, P. Garstecki, and G. M. Whitesides, Synthesis of composite emulsions and complex foams with the use of microfluidic flow-focusing devices, Small **3**, 1792 (2007).

[21] M. Hashimoto and G. M. Whitesides, Formation of bubbles in a multisection flow-focusing junction, Small **6**, 1051 (2010).

[22] M. Hashimoto, S. S. Shevkoplyas, B. Zasońska, T. Szymborski, P. Garstecki, and G. M. Whitesides, Formation of bubbles and droplets in parallel, coupled flow-focusing geometries, Small **4**, 1795 (2008).

[23] J. Ricouvier, P. Tabeling, and P. Yazhgur, Foam as a self-assembling amorphous photonic band gap material, Proc. Natl. Acad. Sci. USA **116**, 9202 (2019).

[24] J. Ricouvier, R. Pierrat, R. Carminati, P. Tabeling, and P. Yazhgur, Optimizing Hyperuniformity in Self-Assembled Bidisperse Emulsions, Phys. Rev. Lett. **119**, 208001 (2017).

[25] E. Y. Arashiro and N. R. Demarquette, Use of the pendant drop method to measure interfacial tension between molten polymers, Mater. Res. **2**, 23 (1999).

[26] Y. Xia and G. M. Whitesides, Soft lithography, Annu. Rev. Mater. Sci. **28**, 153 (1998).

[27] K. Hettiarachchi, E. Talu, M. L. Longo, P. A. Dayton, and A. P. Lee, On-chip generation of microbubbles as a practical technology for manufacturing contrast agents for ultrasonic imaging, Lab Chip **7**, 463 (2007).

[28] A. M. Gañán-Calvo, Perfectly monodisperse microbubbling by capillary flow focusing: An alternate physical description and universal scaling, Phys. Rev. E **69**, 027301 (2004).

[29] P. Garstecki, M. J. Fuerstman, and G. M. Whitesides, Nonlinear Dynamics of a Flow-Focusing Bubble Generator: An Inverted Dripping Faucet, Phys. Rev. Lett. **94**, 234502 (2005).

[30] C. N. Baroud, F. Gallaire, and R. Dangla, Dynamics of microfluidic droplets, Lab Chip **10**, 2032 (2010).

[31] M. T. Sullivan and H. A. Stone, The role of feedback in microfluidic flow-focusing devices, Philos. Trans. R. Soc. A **366**, 2131 (2008).

[32] P. Garstecki, I. Gitlin, W. Diluzio, G. M. Whitesides, E. Kumacheva, and H. A. Stone, Formation of monodisperse bubbles in a microfluidic flow-focusing device, Appl. Phys. Lett. **85**, 2649 (2004).

[33] See Supplemental Material at http://link.aps.org/supplemental/10.1103/PhysRevFluids.5.013602 for (i) symmetric breakup of bubbles Video1; (ii) asymmetric breakup of bubbles Video2; (iii) symmetric breakup of droplets Video3; (iv) asymmetric breakup of droplets Video4.

[34] A. Bedram and A. Moosavi, Droplet breakup in an asymmetric microfluidic T junction, Eur. Phys. J. E **34**, 78 (2011).

[35] M. De Menech, P. Garstecki, F. Jousse, and H. A. Stone, Transition from squeezing to dripping in a microfluidic T-shaped junction, J. Fluid Mech. **595**, 141 (2008).

[36] P. Guillot and A. Colin, Stability of parallel flows in a microchannel after a T junction, Phys. Rev. E **72**, 066301 (2005).

[37] R. Liontas, K. Ma, G. J. Hirasaki, and S. L. Biswal, Neighbor-induced bubble pinch-off: Novel mechanisms of in situ foam generation in microfluidic channels, Soft Matter **9**, 10971 (2013).

[38] P. Garstecki, A. M. Gañán-Calvo, and G. M. Whitesides, Formation of bubbles and droplets in microfluidic systems, Bull. Polish Acad. Sci. **53**, 361 (2005).

[39] D. R. Link, S. L. Anna, D. A. Weitz, and H. A. Stone, Geometrically Mediated Breakup of Drops in Microfluidic Devices, Phys. Rev. Lett. **92**, 054503 (2004).

[40] S. R. Sirsi and M. A. Borden, State-of-the-art materials for ultrasound-triggered drug delivery, Adv. Drug Deliv. Rev. **72**, 3 (2014).

[41] W. Li *et al.*, Microfluidic study of fast gas-liquid reactions, J. Am. Chem. Soc. **134**, 3127 (2012).

[42] M. Versluis, Microbubble acoustic surface cleaning, J. Acoust. Soc. Am. **131**, 3337 (2012).